

Coherent field transients below 15 THz from phase-matched difference frequency generation in 4H-SiC

MARCO P. FISCHER,[†] JOHANNES BÜHLER,[†] GABRIEL FITZKY, TAKAYUKI KURIHARA, STEFAN EGGERT, ALFRED LEITENSTORFER, AND DANIELE BRIDA*

Department of Physics and Center for Applied Photonics, University of Konstanz, 78457 Konstanz, Germany

*Corresponding author: daniele.brida@uni-konstanz.de

We experimentally demonstrate tunable, phase-matched difference frequency generation covering the spectral region below 15 THz using 4H-SiC as a nonlinear crystal. This material combines a non-centrosymmetric lattice and strong birefringence with broadband transparency at low optical frequencies. Thorough refractive index measurements in the terahertz spectral range allow us to calculate phase-matching conditions for any near-infrared pump laser source. 4H-SiC is also exploited as a detector crystal for electro-optic sampling. The results allow us to estimate the effective second-order nonlinear coefficient.

OCIS codes: (190.4400) Nonlinear optics, materials; (320.7110) Ultrafast nonlinear optics; (190.4223) Nonlinear wave mixing; (300.6495) Spectroscopy, terahertz.

The generation of coherent radiation in the spectral region between 5 and 15 THz is a major challenge for solid-state sources, despite its relevant interest for the study of fundamental excitations in condensed matter systems. In fact, the corresponding energy range from 20 to 60 meV includes various molecular vibrations [1–3], as well as optical phonons in solids [4,5] and low-energy collective modes in correlated materials such as superconductors [6]. Quantum cascade lasers [7] provide a continuous wave source tunable in this spectral window. Pulses can also be produced by photoconductive switches [8,9] or via laser-induced air plasma generation [10–12]. However, to obtain stable and intense electric fields combined with femtosecond temporal resolution, the workhorse approach relies on the generation of coherent field transients by frequency mixing processes in nonlinear crystals [13,14]. A typical setup is based on difference frequency generation (DFG) driven by an ultrafast laser system. Unfortunately, in the elusive spectral region between 5 and 15 THz, most nonlinear crystals applied for DFG such as GaSe, AgGaS₂ (AGS), and BBO, exhibit strong optical phonon resonances that lead to

reststrahlen bands where radiation cannot penetrate into the material [see Fig. 1(a)]. In addition, isotropic materials such as ZnTe are lacking birefringence and, therefore, do not allow adjustment of phase matching. Furthermore, organic nonlinear crystals [15] show heavily structured spectra in the frequency range of interest and display inherently low damage thresholds. Recently, preliminary investigations by Naftaly *et al.* [16] suggested 4H-SiC as a crystal suitable for nonlinear optics in the multi-terahertz range. So far, this outstanding material has received little attention in experimental works that are limited to the demonstration of nonlinear properties in the near infrared [17], mid-infrared DFG above the optical phonon frequencies [18], and emission of 1 THz radiation from 6H-SiC [19].

In this Letter, we experimentally demonstrate the application of 4H-SiC for the generation of ultrashort field transients tunable between 5 and 15 THz, and its use as an electro-optic sampling (EOS) crystal.

SiC exhibits a large plurality of polymorphs with hexagonal, cubic, and rhombohedral symmetry [20]. Owing to its technological relevance, high-quality synthetic crystals of 4H-SiC are available. Its lattice, sketched in Fig. 1(b), is characterized by an ABCB stacking order of four hexagonal Si-C bilayers (space group C_{6v}⁴ – P6₃mc [20], point group 6mm [21]). This polymorph is preferred over alternatives such as 6H-SiC (ABCACB) and 3C-SiC (ABC, cubic) due to its stronger positive uniaxial birefringence [22]. 4H-SiC has two broad transmission windows, one spanning the visible and near infrared [Fig. 2(a)], the other extending from 18 THz (16 μm) down to the sub-terahertz range [Fig. 2(b)] owing to the high phonon frequencies of the Si-C dimers [23]. Among the most prominent features, we can also list a high second-order nonlinearity [19,24,25], excellent mechanical robustness (Mohs hardness 9 [26]), and outstanding thermal properties. The decomposition temperature is 2830°C [27], and the thermal conductivity of 490 W m⁻¹ K⁻¹ is surpassed only by diamond [21]. In contrast to layered materials such as GaSe, SiC crystals can be cut and polished in any crystal direction to exploit the birefringence for phase matching at normal incidence. In addition, the large bandgap of 3.3 eV [20] prevents two-photon

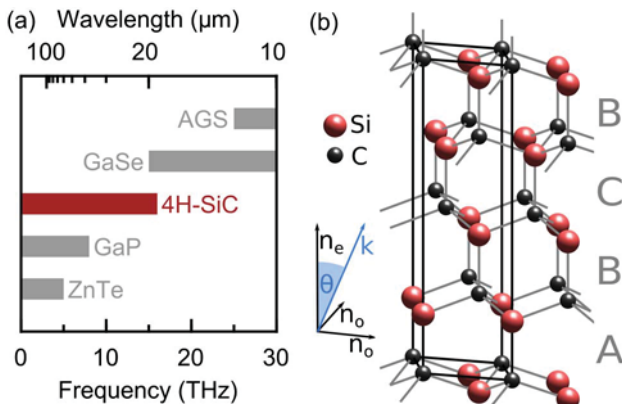


Fig. 1. (a) Comparison of the operation range of widely used nonlinear crystals for DFG. (b) Section of the 4H-SiC crystal lattice (space group $C_{6v}^4 - P6_3mc$) consisting of four hexagonal bi-layers of Si and C (red and black, respectively) with a stacking order ABCB. The optical axis (n_o) is parallel to the long face of the unit cell, as sketched in the inset. The propagation angle θ is calculated with respect to this direction.

absorption by near-infrared beams down to Ti:sapphire laser wavelength allowing for intense optical pumping.

Bulk semi-insulating 4H-SiC crystals grown by high-temperature chemical vapor deposition [28] were obtained from Norstel AB (Sweden). The samples for the nonlinear experiments were diamond-cut and polished at several angles θ with respect to the optical axis [see Fig. 1(b)]. We produced several specimens for type-I phase matching at angles $\theta = 0^\circ, 30^\circ, 45^\circ$, and 90° with optical apertures of 5 mm and thicknesses ranging from 100 to 500 μm . Under our experimental conditions, the useful crystal thickness is limited to approximately 500 μm by the group velocity mismatch of the three interacting femtosecond pulses.

The dielectric function for both ordinary (o) and extraordinary (e) polarization directions was characterized from 1 to 18 THz by means of time-domain spectroscopy (TDS). The characterization relies on EOS in 19 μm thick ZnTe with gating pulses that are shorter than 10 fs to ensure the precise detection of frequencies up to 40 THz [29]. The birefringent refractive index can be described with two distinct Sellmeier equations separated by the reststrahlen band for the near infrared [obtained by Wang *et al.* [18] and Fig. 2(c)] and for the far infrared according to the fitting of our TDS measurements with Eqs. (1) and (2) [also plotted in Fig. 2(d)], together with the experimental data:

$$n_{e,\text{THz}}^2 = 7.346 + \frac{3.026 \cdot \lambda^2}{\lambda^2 - 175.2}, \quad (1)$$

$$n_{o,\text{THz}}^2 = 7.055 + \frac{2.669 \cdot \lambda^2}{\lambda^2 - 167.8}, \quad (2)$$

where the wavelength λ is in μm . These refractive index dispersions differ slightly from previously reported values [16] and provide a better description of the phase-matching conditions that we observe.

Phase-matching angles based on the refractive index data have been calculated for pump wavelength λ_p and target idler emission wavelength λ_i of the DFG process. The

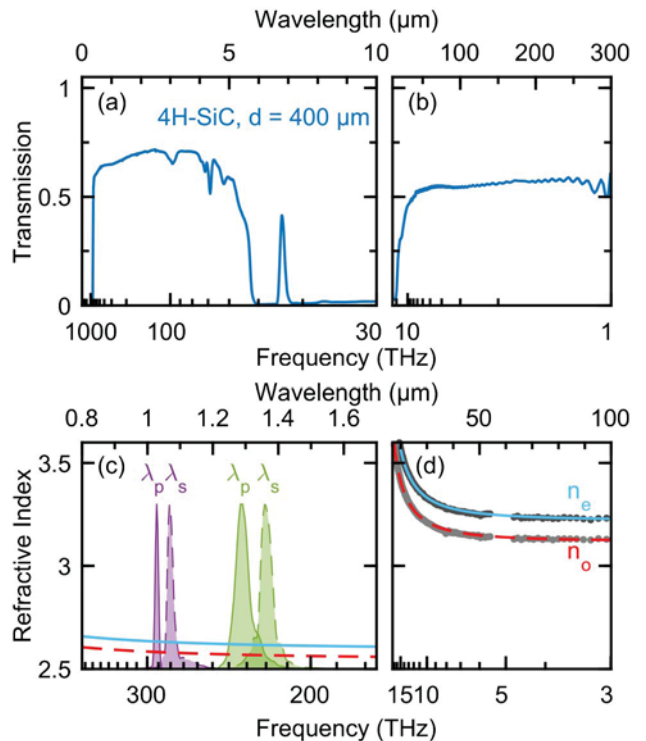


Fig. 2. (a) and (b) Transmission spectrum of a 400 μm thick 4H-SiC sample ($\theta = 0^\circ$). It features (a) a broad transparency from 370 to 6 μm followed by reststrahlen and multi-phonon absorption bands between 18 THz and 50 THz and (b) high transmissivity in the terahertz frequency window. Transmission is limited to 0.5 only by Fresnel losses which may be avoided with an anti-reflection coating. (c) Near-IR refractive index (ordinary and extraordinary) of 4H-SiC according to Wang *et al.* [18], including normalized pump (solid line) and signal (dashed line) spectra used for DFG in the two experimental setups. (d) Far-IR refractive index obtained by TDS measurements (dots) and corresponding Sellmeier fit (n_e as solid line, n_o as dashed line), according to Eqs. (1) and (2).

corresponding frequency mixing is then described by $\lambda_i^{-1} = \lambda_p^{-1} - \lambda_s^{-1}$, where λ_s is the signal wavelength seeded together with the pump beam.

For the crystal symmetry group of 4H-SiC, only type-I (ooe) phase matching is possible in the desired spectral range. The effective nonlinearity is $\chi_{\text{eff}}^{(2)} = \chi_{31}^{(2)} \cdot \sin(\theta)$, since Kleinmann symmetry is not valid in this case [30]. Panels (a) in Figs. 3 and 4 report the calculation of the phase-matching angle corresponding to the generation of a target idler frequency for $\lambda_p = 1025$ and 1280 nm, respectively. Shorter pump wavelengths allow us to reach higher idler frequencies with the maximum being limited by the diverging refractive index close to the onset of the transverse optical phonon resonance at 18 THz. A comparison of both calculations also illustrates the influence of crystal thickness on the idler bandwidth.

Two high-power femtosecond laser systems, one based on a Ti:sapphire amplifier seeded by a femtosecond Er:fiber front-end and one Yb:KGW-based system, are used to demonstrate DFG for different pump wavelengths. The Ti:sapphire system operates at a repetition rate of 1 kHz. It is equipped with two optical parametric amplifiers (OPAs), each delivering 250 μJ pulses [29,31] tuned to central wavelengths of

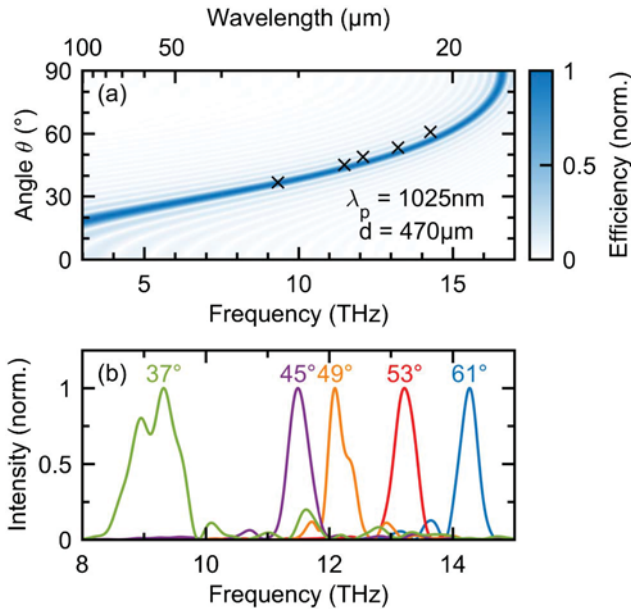


Fig. 3. (a) Phase matching for crystal angles θ as a function of the target idler frequency showing the calculated efficiency (color scale) for $\lambda_p = 1025$ nm. (b) Pulse spectra obtained by tuning the phase-matching angle θ between 37° and 61° (crosses in the upper panel) in $470\mu\text{m}$ thick 4H-SiC cut at 45° with $\lambda_p = 1025$ nm. The transient characterization was performed by EOS in a $30\mu\text{m}$ thick ZnTe crystal.

$\lambda_p = 1280$ nm and $\lambda_s = 1350$ nm [green shaded spectra Fig. 2(c)]. The Yb:KGW system works at 50 kHz repetition rate. It is designed to generate the difference frequency between the fundamental laser pulse at $\lambda_p = 1025$ nm ($45\mu\text{J}$ pulse energy) and the output of a tunable OPA ($\lambda_s \approx 1080$ nm, $2.0\mu\text{J}$ pulse energy) focused collinearly on the nonlinear crystal [purple shaded spectra in Fig. 2(c)].

In both systems, Ge long-pass filters block the near-infrared light after the SiC crystals. Nitrogen purging is implemented to prevent absorption by water vapor and CO_2 resonances of ambient air. The phase-stable multi-terahertz transients are detected via EOS in $30\mu\text{m}$ thick [110]-ZnTe providing a broadband detection window up to 30 THz [32]. Alternatively, 4H-SiC has also been used as a detector crystal when the DFG spectra overlap with the ZnTe reststrahlen band between 5 and 8 THz.

Panels (b) in Figs. 3 and 4 show the spectra of the transients generated at various phase-matching angles achieved by using the two generation systems. The multi-terahertz frequencies measured in the experiments coincide with the calculated phase-matching condition at the respective angles [crosses in Figs. 3(a) and 4(a)]. In both cases, it is possible to obtain a broad tunability range below 15 THz.

4H-SiC can also be the nonlinear crystal for EOS, as mentioned in the case of the transients tuned where ZnTe is not applicable. Figures 5(a) and 5(b) show the field trace and intensity spectrum centered at 1.5 THz of a transient generated by optical rectification in $500\mu\text{m}$ thick ZnTe. This EOS characterization is performed with a $400\mu\text{m}$ thick 4H-SiC sample cut at 0° and tilted to $\theta = 10^\circ$ to optimize phase matching and nonlinearity.

A typical field transient generated in 4H-SiC at a phase-matching angle of 45° and $\lambda_p = 1280$ nm is shown in

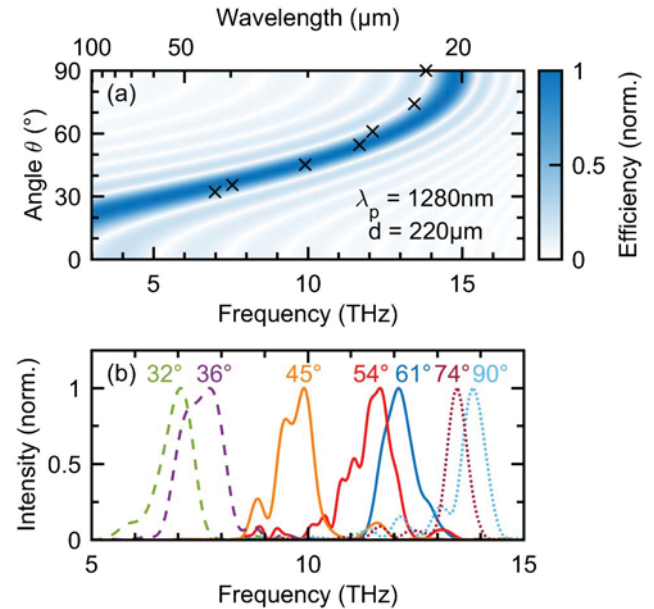


Fig. 4. (a) Phase matching for crystal angles θ as a function of the target idler frequency showing the calculated efficiency (color scale) for $\lambda_p = 1280$ nm. (b) Pulse spectra obtained for $\lambda_p = 1280$ nm by tuning the phase-matching angle θ between 32° and 61° (solid and dashed lines) and between 74° and 90° in a $330\mu\text{m}$ thick sample cut at 90° (dotted lines). The transient characterization was performed by EOS in a $30\mu\text{m}$ thick ZnTe crystal for all the spectra except for the two plotted with dashed lines, where a $470\mu\text{m}$ thick 4H-SiC was employed to avoid the ZnTe reststrahlen band.

Fig. 5(c). Both ZnTe (thickness $L_{\text{ZnTe}} = 30\mu\text{m}$, solid line in the figure) and 4H-SiC ($L_{\text{SiC}} = 470\mu\text{m}$, $\theta = 45^\circ$, dashed line) can be employed for characterization of the 10 THz pulses by EOS. The two detection schemes show equivalent normalized electric field traces which may be directly compared. The phase-matching restriction of the $470\mu\text{m}$ thick 4H-SiC crystal results in a slightly narrower spectral bandwidth [Fig. 5(d)]. The maximum relative polarization rotation achieved with 4H-SiC is $\Delta I_{\text{SiC}}/\Delta I_{\text{ZnTe}} = 21\%$ of the value measured with the ZnTe crystal. From this, the effective electro-optic coefficient $r_{\text{eff},\text{SiC}} = r_{31,\text{SiC}} \cdot \sin(\theta)$ can be determined as

$$r_{\text{eff},\text{SiC}} = \frac{\Delta I_{\text{SiC}}}{\Delta I_{\text{ZnTe}}} \cdot \frac{L_{\text{ZnTe}}}{L_{\text{SiC}}} \cdot \frac{\int I_g(\lambda) \lambda / [n_{\text{SiC}}^3(\lambda) \cdot G_{\text{SiC}}] d\lambda}{\int I_g(\lambda) \lambda / [n_{\text{ZnTe}}^3(\lambda) \cdot G_{\text{ZnTe}} \cdot r_{41,\text{ZnTe}}(\lambda)] d\lambda}, \quad (3)$$

with the specific electro-optic response functions G_{SiC} and G_{ZnTe} , the gate spectrum $I_g(\lambda)$, and the well-known frequency-resolved electro-optic coefficient $r_{41,\text{ZnTe}}(\lambda)$ of ZnTe [32–34]. The second-order susceptibility of 4H-SiC is thus estimated to be

$$|\chi_{31}^{(2)}| = \frac{1}{2} |r_{31}| \cdot n^4 \approx 8.5 \text{ pm/V}, \quad (4)$$

in agreement with previous measurements [24]. This relatively small value is counterbalanced by the efficiency gain by the applicability of thick crystals enabled through birefringent

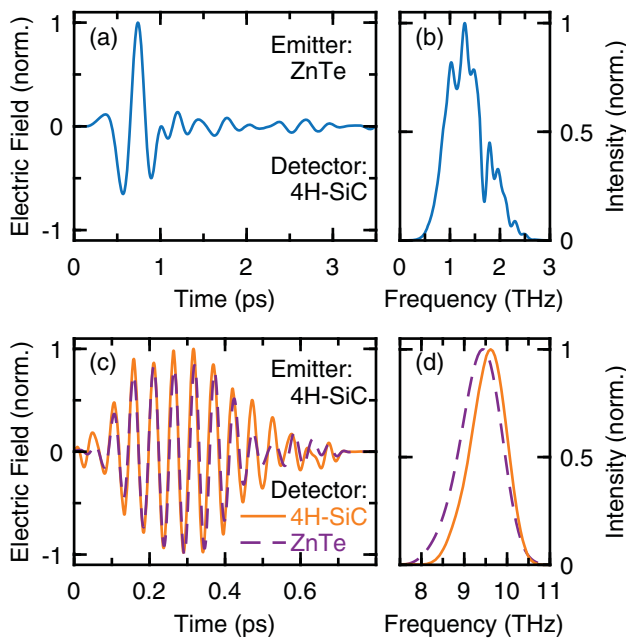


Fig. 5. (a) EOS time trace of a broadband pulse centered at 1.5 THz generated via optical rectification in [110]-ZnTe recorded using 4H-SiC as a detection crystal (thickness 400 μm , $\theta = 10^\circ$). (b) Calculated spectral intensity. (c) EOS time traces of a field transient generated via DFG in 4H-SiC (thickness 220 μm , $\theta = 45^\circ$, $\lambda_p = 1280 \text{ nm}$) recorded with [110]-ZnTe (dashed line, thickness 30 μm) and 4H-SiC (solid line, thickness 470 μm , $\theta = 45^\circ$), respectively. (d) Calculated spectral intensity of both EOS field transients.

phase matching as opposed to ZnTe where this is not possible. In addition, by comparing the electro-optic polarization rotation with stronger field transients generated at the low-frequency limit of GaSe of 16 THz, we estimate that the peak electric fields generated in 4H-SiC are in the order of 5 kV/cm. While this value is not suitable for driving strong field experiments, it is by far sufficient for the probing of resonant phenomena in condensed matter.

In conclusion, we demonstrate that semi-insulating 4H-SiC complements established nonlinear crystals by allowing the generation of coherent transients covering the frequency range between 5 and 15 THz that was previously inaccessible by solid-state nonlinear sources. Importantly, the strong birefringence and excellent transmission allow full tunability both in difference frequency generation and in electro-optic detection. SiC is a promising material for the generation of pulses in a frequency range that allows us to investigate fundamental ultrafast processes in molecules, correlated materials, perovskites and highly doped semiconductors.

Funding. Seventh Framework Programme (FP7) (613055); Deutsche Forschungsgemeinschaft (DFG) (BR 5030/1-1); Carl-Zeiss-Stiftung.

Acknowledgment. The authors thank Björn Magnusson (Norstel AB, Sweden) for kindly supplying high-quality bulk 4H-SiC crystals.

[†]These authors contributed equally to this Letter.

REFERENCES

- G. Herzberg, *Molecular Spectra and Molecular Structure. II. Infrared and Raman Spectra of Polyatomic Molecules*, 2nd ed. (Van Nostrand, 1945).
- F. Perakis, L. De Marco, A. Shalit, F. Tang, Z. R. Kann, T. D. Kühne, R. Torre, M. Bonn, and Y. Nagata, *Chem. Rev.* **116**, 7590 (2016).
- J. Petersen, K. B. Møller, R. Rey, and J. T. Hynes, *J. Phys. Chem. B* **117**, 4541 (2013).
- A. I. Lebedev, *Phys. Solid State* **51**, 362 (2009).
- Y. Yang, D. P. Ostrowski, R. M. France, K. Zhu, J. van de Lagemaat, J. M. Luther, and M. C. Beard, *Nat. Photonics* **10**, 53 (2015).
- A. Pashkin, M. Porer, M. Beyer, K. W. Kim, A. Dubroka, C. Bernhard, X. Yao, Y. Dagan, R. Hackl, A. Erb, J. Demsar, R. Huber, and A. Leitenstorfer, *Phys. Rev. Lett.* **105**, 67001 (2010).
- K. Ohtani, M. Beck, M. J. Süess, J. Faist, A. M. Andrews, T. Zederbauer, H. Detz, W. Schrenk, and G. Strasser, *ACS Photon.* **3**, 2280 (2016).
- A. Leitenstorfer, S. Hunsche, J. Shah, M. Nuss, and W. Knox, *Phys. Rev. B* **61**, 16642 (2000).
- P. J. Hale, J. Madeo, C. Chin, S. S. Dhillon, J. Mangeney, J. Tignon, and K. M. Dani, *Opt. Express* **22**, 26358 (2014).
- I.-C. Ho, X. Guo, and X.-C. Zhang, *Opt. Express* **18**, 2872 (2010).
- T. Wang, K. Iwaszcuk, E. A. Wrisberg, E. V. Denning, and P. U. Jepsen, *J. Infrared Millim. Terahertz Waves* **37**, 592 (2016).
- Y. Minami, T. Kurihara, K. Yamaguchi, M. Nakajima, and T. Suemoto, *Appl. Phys. Lett.* **102**, 151106 (2013).
- A. Pashkin, F. Junginger, B. Mayer, C. Schmidt, O. Schubert, D. Brida, R. Huber, and A. Leitenstorfer, *IEEE J. Sel. Top. Quantum Electron.* **19**, 8401608 (2013).
- M. C. Hoffmann and J. A. Fülop, *J. Phys. D* **44**, 83001 (2011).
- A. Schneider, M. Neis, M. Stillhart, B. Ruiz, R. U. A. Khan, and P. Günter, *J. Opt. Soc. Am. B* **23**, 1822 (2006).
- M. Naftaly, J. F. Molloy, B. Magnusson, Y. M. Andreev, and G. V. Lanskii, *Opt. Express* **24**, 2590 (2016).
- P. M. Lundquist, W. P. Lin, G. K. Wong, M. Razeghi, and J. B. Ketterson, *Appl. Phys. Lett.* **66**, 1883 (1995).
- S. Wang, M. Zhan, G. Wang, H. Xuan, W. Zhang, C. Liu, C. Xu, Y. Liu, Z. Wei, and X. Chen, *Laser Photon. Rev.* **7**, 831 (2013).
- J. H. Strait, P. A. George, J. Dawlaty, S. Shivaraman, M. Chandrashekhar, F. Rana, and M. G. Spencer, *Appl. Phys. Lett.* **95**, 51912 (2009).
- G. L. Harris, *Properties of Silicon Carbide* (INSPEC, the Institution of Electrical Engineers, 1995).
- M. Weber, *Handbook of Optical Materials* (CRC Press, 2002).
- P. T. Shaffer, *Appl. Opt.* **10**, 1034 (1971).
- A. Paarmann, I. Razdolski, A. Melnikov, S. Gewinner, W. Schöllkopf, and M. Wolf, *Appl. Phys. Lett.* **107**, 81101 (2015).
- S. Niedermeier, H. Schillinger, R. Sauvrebrey, B. Adolph, and F. Bechstedt, *Appl. Phys. Lett.* **75**, 618 (1999).
- H. Sato, M. Abe, I. Shoji, J. Suda, and T. Kondo, *J. Opt. Soc. Am. B* **26**, 1892 (2009).
- C.-M. Zetterling, *Process Technology for Silicon Carbide Devices* (INSPEC, the Institution of Electrical Engineers, 2002).
- R. I. Scace and G. A. Slack, *J. Chem. Phys.* **30**, 1551 (1959).
- A. Ellison, B. Magnusson, N. T. Son, L. Storasta, and E. Janzen, *Mater. Sci. Forum* **433–436**, 33 (2003).
- F. Junginger, A. Sell, O. Schubert, B. Mayer, D. Brida, M. Marangoni, G. Cerullo, A. Leitenstorfer, and R. Huber, *Opt. Lett.* **35**, 2645 (2010).
- F. Zernike and J. E. Midwinter, *Applied Nonlinear Optics* (Wiley, 1973).
- D. Brida, C. Manzoni, G. Cirmi, M. Marangoni, S. Bonora, P. Villaresi, S. De Silvestri, and G. Cerullo, *J. Opt.* **12**, 13001 (2010).
- A. Leitenstorfer, S. Hunsche, J. Shah, M. C. Nuss, and W. H. Knox, *Appl. Phys. Lett.* **74**, 1516 (1999).
- G. Gallot and D. Grischkowsky, *J. Opt. Soc. Am. B* **16**, 1204 (1999).
- Q. Wu and X.-C. Zhang, *Appl. Phys. Lett.* **71**, 1285 (1997).